

RESEARCH ARTICLE | APRIL 12 2021

Reconfigurable plasma-dielectric hybrid photonic crystal as a platform for electromagnetic wave manipulation and computing

Benjamin Wang; Jesse A. Rodríguez ; Oliver Miller; Mark A. Cappelli  

 Check for updates

Physics of Plasmas 28, 043502 (2021)

<https://doi.org/10.1063/5.0043336>

 CHORUS

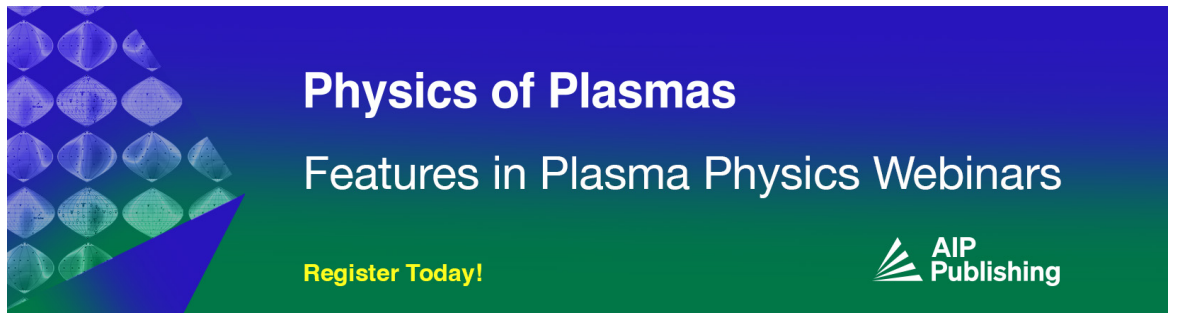


View Online




Export Citation

CrossMark

Physics of Plasmas
Features in Plasma Physics Webinars

Register Today!



Reconfigurable plasma-dielectric hybrid photonic crystal as a platform for electromagnetic wave manipulation and computing

Cite as: Phys. Plasmas **28**, 043502 (2021); doi: [10.1063/5.0043336](https://doi.org/10.1063/5.0043336)

Submitted: 7 January 2021 · Accepted: 17 March 2021 ·

Published Online: 12 April 2021



View Online



Export Citation



CrossMark

Benjamin Wang,^{a)} Jesse A. Rodríguez,^{b)}  Oliver Miller,^{c)} and Mark A. Cappelli^{d)} 

AFFILIATIONS

Department of Mechanical Engineering, Stanford University, Stanford, California, 94305, USA

^{a)}Electronic mail: bwang17@stanford.edu

^{b)}Electronic mail: jrodrig@stanford.edu

^{c)}Electronic mail: metroid@stanford.edu

^{d)}Author to whom correspondence should be addressed: cap@stanford.edu

ABSTRACT

The introduction of 3D printing has enabled fabrication of photonic crystal devices with complex crystal structures that would be challenging to construct using other fabrication methods. In this paper, we construct and characterize a photonic crystal consisting of two $4 \times 8 \times 8$ cubic lattices composed of spherical silicon nitride elements straddling a layer of 8 plasma discharge tubes, creating a 3D hybrid plasma photonic crystal device. Integrating under-dense gaseous plasma elements provides a unique coupling dynamic between the dielectric spheres and the cylindrical plasma discharges, creating a monolithic hybrid photonic crystal with solid state and reconfigurable elements. The device has resonant modes that have attenuation peaks that are either switchable, tunable in amplitude, or tunable in frequency with variations in plasma density. The response of these bands seen with varying plasma density is confirmed through simulations when effects due to the heating of the photonic crystal from the gaseous plasma elements are accounted for in the experiments. We discuss how this reconfigurable device may be used and expanded upon for applications in photonic artificial neural networks and optical computing systems.

Published under license by AIP Publishing. <https://doi.org/10.1063/5.0043336>

I. INTRODUCTION

Future computing platforms will manipulate electromagnetic (EM) waves in some form to carry out computational tasks.¹ Optical computing affords a higher bandwidth and speed in comparison to its solid state electronic counterpart and is less prone to component heating as it is not subject to direct Ohmic losses. In their most primitive form, the earliest optical computers will likely contain discrete photonic devices that mimic traditional electronics-based circuit elements such as the transistor² and will carry out computational tasks very much like that in modern electronic processors. In modern electronic architectures, tasks such as the multiplication of numbers can be quite involved, requiring multiple systematic steps that manipulate (shift and add) binary digits—a process that benefits from parallel algorithms. However, optical computing using these familiar schemes will eventually encounter architecture limitations.

One alternative computational architecture is the artificial neural network (ANN).³ Artificial neural networks can be thought of as computer automata, using machine learning to carry out state-specific

tasks, inspired by the processes that are believed to occur in the human brain. Artificial neural networks can be constructed using photonic components,^{4–6} with various computational architectures that enable the analysis of large data sets that lie within the training window in single processing events. The development of such computational platforms will likely require a completely new set of photonic devices that control the phase, amplitude, and transmission of EM waves. One platform that has been proposed recently is an analog EM wave processor consisting of an inhomogeneous nonlinear artificial material.⁷ Another platform that has been proposed is for applications where inputs and hence the complex information are encoded spatially into the source wavefront.⁵ Wave-based operators such as metamaterials or photonic crystals can be trained as recurrent neural networks, giving them temporal dynamic behavior enabling the passive processing of signals without analog-to-digital conversion greatly increasing computational speed. Enhancements in performance can be obtained if the spatial properties of the artificial materials can be dynamically controlled, and prior work has shown some of these materials to be weakly

reconfigurable.^{8,9} Artificial neural networks can exploit nonlinear¹⁰ and directional anisotropies¹¹ of photonic crystals. An optimum meta-material or photonic crystal would be one that offers full 3D phase and amplitude control of EM wavefronts through reconfigurability while able to tolerate high wave energy thresholds for nonlinearities. In this paper, we present a 3D photonic crystal with embedded plasma elements as a possible candidate for such platforms. The EM response of complex 3D photonic crystals has been studied extensively. Added plasma elements enable tunability and dynamic reconfigurability at potentially high speeds¹²—features that are not readily present in conventional solid-state photonic crystals. At sufficiently high incident field intensities, the plasma response is also nonlinear owing to the field-dependent plasma density which controls the plasma dielectric constant.

The device presented in this paper operates in the Ka band (26.5–40 GHz) and requires the use of materials that have dielectric constants and loss tangents appropriate for designing a device that can have proper wave coupling and photonic and resonant effects. As described below, we use 3D printing for the fabrication of a scaffold to assemble a 3D Si_2N_3 photonic crystal with embedded plasma elements. Scaffolds can be made out of a variety of 3D printable materials, most commonly PLA (polylactic acid) or nylon, but more exotic materials have been printed including carbon fiber,¹³ conductive plastics,¹⁴ and flexible thermoplastics.¹⁵ The printing of high dielectric constant ceramics is still the subject of much research and is not readily available in commercial devices. Here, we employ the scaffold to hold and confine the Si_2N_3 spherical elements and gas discharge plasma rods. The plasma discharge tubes, placed in the center of the crystal, provide a potentially dynamic coupling layer that alters the transmission properties. Here, because of the high wave frequencies, the plasma density in the tubes is significantly underdense and the wave manipulation is subtle yet reproducible. As shown below, this hybrid device, therefore, operates as a single reconfigurable and tunable processor of EM waves.

The use of gaseous plasma elements to allow for tunability in photonic crystal devices has been explored in previous works.^{16–19} Gaseous plasma discharges as elements of photonic crystals present a frequency-dependent permittivity often modeled using the Drude approximation. Both positive and negative dielectric constants are accessible when operating frequencies are in the vicinity of the plasma frequency, ω_p , although for applications where wavelengths smaller than the photonic crystal size may be desirable, operation well above the plasma frequency may be unavoidable. These significantly underdense plasmas, therefore, have a dielectric constant very close to unity. This regime has a significantly different physics than the negative dielectric constant regime and it is important to understand the photonic crystal response of this regime for possible applications. In this permittivity regime, the wavelengths are increased within the plasma due to the refractive index being less than 1, yet real, which is different than the negative dielectric constant regime that is often studied in metals and also in overdense plasma photonic crystal systems. The need to understand how to utilize underdense plasmas and to characterize the subtle response is of importance due to the difficulties of scaling the plasma density upwards as feature sizes decrease at higher device operating frequencies.

The design of the 3D hybrid photonic crystal combines two solid state photonic crystals with a single layer of individually addressable

plasma elements that can be switched on and off and also tuned in plasma density. The current design has deep bandgap structures that are due to the two dielectric 3D photonic crystal sections, which are coupled by a single layer of underdense plasma rods. This configuration has been explored theoretically for tuning the existence of exceptional points in optical photonics.²⁰ In future work, we will explore the effect of changing the configuration of the plasma density and “on-off” states of the system in order to understand the phase and amplitude mapping of various configurations, allowing for computing systems with “one-shot” execution²¹ to be designed and explored. The use of plasma elements can also act as activation functions in optical neural networks. If there is energy coupling between the source input and the plasma, changing parameters such as the plasma frequency would allow nonlinear transmission features into the system.²² Unlike solid state elements which can suffer irreversible damage at high intensity, plasmas are unique in that they have a field-dependent permittivity and are self-healing.

II. PHOTONIC CRYSTAL DESIGN AND CONSTRUCTION

Figure 1 provides an experimental diagram of the photonic crystal and surrounding microwave source and receiver. Two horn antennas (A-Info LB-180400–15-A, 18.0–40 GHz) were used as the source and detector, spaced 45 cm apart, with the E-field polarized along the y-axis, transverse to the axis along the plasma cylinders. Teflon lenses (Thorlabs LAT151, $f = 151.1$ mm) were positioned at an object and image distance of 4 cm to assist with focusing and collecting the EM waves. Microwave absorbing foam (ARC Technologies RT foam) was placed around the horn antenna apertures to reduce spurious reflections. The antennas are connected to an HP 8722D vector network analyzer to measure the S-parameters, particularly S_{21} , which represents the EM wave transmission through the crystal. The measurements were acquired with an integration time of 5 ms per frequency point (1601 points per scan from 18 to 40 GHz), with the source power set at -5 dBm. At this level, we anticipate that the interactions

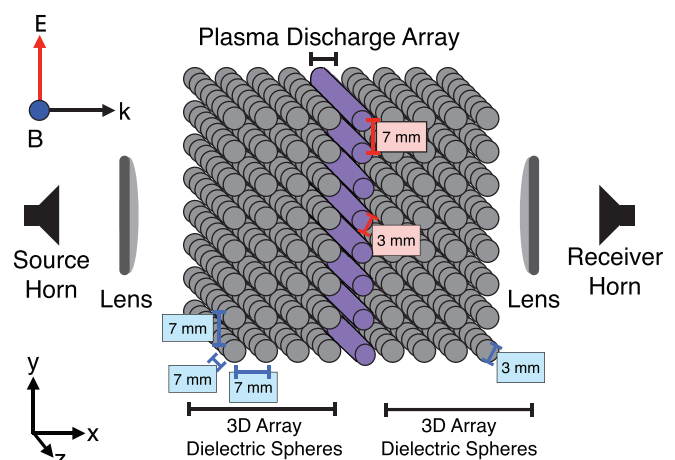


FIG. 1. Schematic of hybrid 3D plasma photonic crystal consisting of two silicon-nitride 3D photonic crystals coupled with a layer of 8 plasma discharge tubes. Note the PLA scaffold is not shown in this schematic, but the PLA is included both experimentally and in simulations.

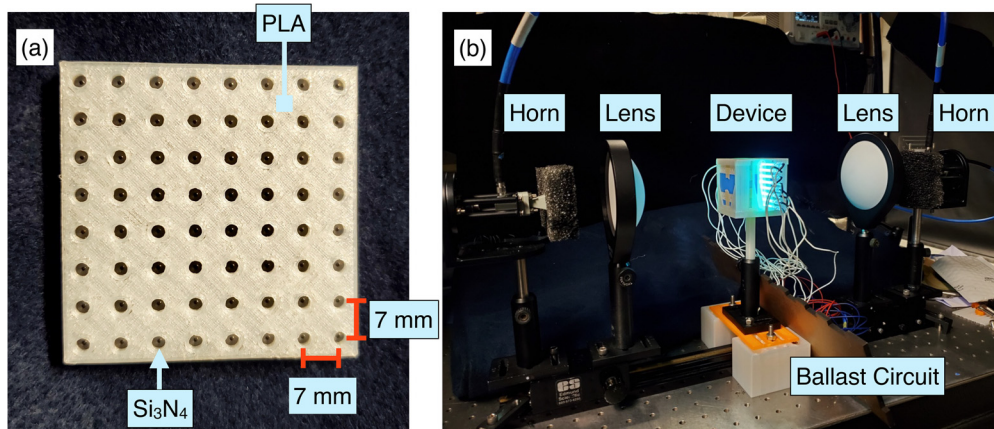


FIG. 2. (a) Single layer PLA 3D printed scaffold with embedded silicon-nitride (Si_3N_4) spheres ($d = 3$ mm). (b) Full experimental measurement setup with microwave horns, microwave absorbing foam, lens, and photonic crystal with embedded plasmas.

between the EM wave and low density plasma elements will be in the linear regime.

The dielectric photonic crystal consists of silicon-nitride spheres ($d = 3$ mm) that are placed in a 3D printed PLA scaffold. The 3D printed scaffolds were fabricated using a commercially available 3D printer (Flashforge Creator Pro dual extruder) and printed using PLA filament (3D Solutech Natural Clear 1.75 mm). The printer has a nozzle diameter of 0.4 mm and is capable of depositing a layer thickness of 0.1–0.3 mm. The scaffold in Fig. 2(a) consists of a top and bottom 3D printed structure that holds the silicon-nitride spheres in position. Each of these layers is removable and can be stacked for different configurations for future experiments.

The plasma layer was fabricated using a 3D printed scaffold that allowed each of the rods to be tightly fitted in the same lattice spacing. A 3D printed monolith scaffold was used to enclose the silicon-nitride and plasma layers, designed to allow maximum exposure of the collimated EM beam. We found it important to have tight tolerances for each of the scaffolds so that each of the layers does not shift or move and that the lattice spacing is consistent throughout the device.

Silicon nitride has a reported dielectric constant, ϵ_D , between 7 and 12.²³ We determined our silicon nitride spheres to have a value of $\epsilon_D = 12$ by simulating the silicon nitride photonic crystal and PLA ($\epsilon = 2.5$) scaffold with no plasma elements, and matching the measured transmission to that of ANSYS high frequency structure simulator (HFSS) simulations for various values of ϵ_D .

The plasma array consists of eight individual quartz discharge tubes (overall length = 130 mm, visible plasma length = 120 mm, outer quartz diameter = 3 mm, quartz wall thickness = 0.75 mm, and plasma diameter ≈ 1.5 mm) filled with argon and mercury. The plasma discharges are driven by individual AC ballasts. Nominal operation resulted in near triangular voltage and current waveforms that were essentially in-phase (resistive loads) with a peak-to-peak voltage and current of 1060 V and 24.52 mA, respectively, at 47.38 kHz. The ballast output can be controlled using a programmable input voltage to examine the system transmission to varying discharge power and hence plasma density. As varying power changes the quartz tube and surrounding scaffold temperature, the outer temperature of the quartz envelope is measured with a Raytek MiniTemp infrared thermometer.

Transmission measurements were made when a temperature of $T = 23.5^\circ\text{C}$ is reached from a cold start of the discharge. In a typical experiment and at nominal discharge conditions, this temperature is reached in approximately 5 s. The discharge was allowed to cool to room temperature after each measurement. Figure 2(b) shows the experimental setup with the two horn antennas, focusing lenses, device, and ballast circuit. A closeup of the complete device is shown in Fig. 3.

A plasma discharge model was used to estimate the experimental plasma densities. The online electron energy distribution solver, BOLSIG+,^{24,25} was used to estimate the plasma parameters, particularly n_e and the electron-atom momentum scattering collision frequency, γ_p . These parameters and plasma tube geometry served as inputs to HFSS simulations of the transmitted response of the device. The modeled volume-average electron density is derived from

$$n_e = \frac{I_{RMS}}{eA\mu_d},$$

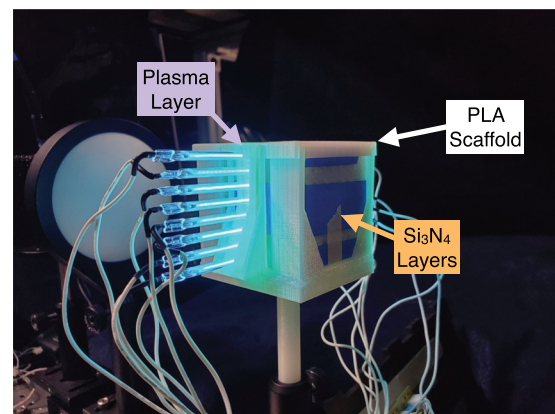


FIG. 3. Hybrid 3D plasma photonic crystal device with plasma layer, Si_3N_4 layers, in a 3D printed PLA scaffold.

where I_{RMS} is the measured RMS current, $A = \pi d^2/4$ is the inside cross-sectional area of the discharge tube with $d = 1.5$ mm, μ_d is the electron mobility, and e the fundamental electron charge. The BOLSIG+ simulations provide electron mobility and require an estimate of the time-averaged reduced electric field (E/N). The electric field, E , is determined from V_{RMS} , which, for the nominal conditions, is 303.1 V (corrected for an estimated cathode fall voltage of approximately 10 V²⁶) and the approximate length of the visible discharge positive column (determined from images obtained with a CCD camera) $L_d = 120$ mm. The major uncertainty in estimating the reduced field is the lack of knowledge of the total gas pressure (or total species number density, N) in the discharge tube, as the fill conditions of the lamps, typically argon with saturated mercury is proprietary. These germicidal discharge lamps usually have argon fill pressure that ranges from about 25 Pa (100 mTorr) to several hundreds of Pascals at room temperature (300 K), and when operating, increase in temperature to about 315 K.²⁷ We assume a peak-to-peak voltage and current of 1060 V and 24.52 mA, respectively, at 47.38 kHz for use in the BOLSIG+ simulations. At this temperature, the equilibrium vapor pressure of mercury is about 1 Pa, much less than that of argon. At operating temperature, the reduced fields for the generous range of possible fill pressures²⁸ of 300 to 25 Pa correspond to 34.8 to 956.3 Td, respectively. For this range, the BOLSIG+ simulations (Ar, Hg cross section for species e from SIGLO) indicate a possible range of plasma density of 7×10^{11} to 4.25×10^{10} cm⁻³, corresponding to a plasma frequency

$$\omega_p = \sqrt{\frac{n_e e^2}{m_e \epsilon_0}},$$

ranging from 1.85 to 7.50 GHz. In this equation, m_e is the electron mass and ϵ_0 is the free space permittivity. Over this range, the electron momentum scattering frequency is expected to vary from 0.6 to 9.0 GHz. Figure 4 plots the BOLSIG+ calculated plasma frequency and collision scattering frequency for the range of possible argon fill pressures. Below we describe experiments and HFSS simulations of

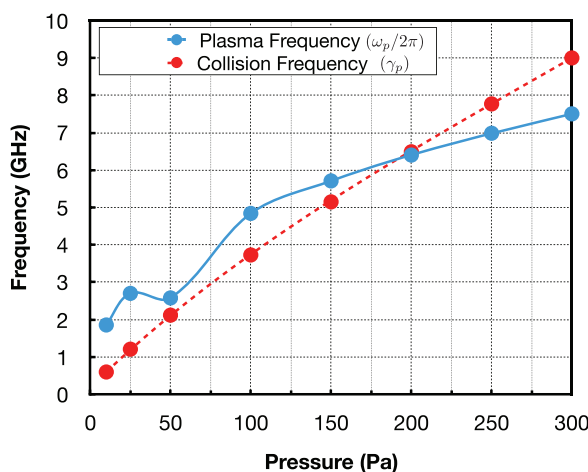


FIG. 4. BOLSIG+ simulations of the experimental discharge of the plasma frequency (GHz) as a function of fill gas pressure (Pa) from 25 to 300 Pa, corresponding to a reduced electric field (E/N) from 956.3 to 34.8 Td.

transmission assuming this range of plasma conditions. The plasma elements are modeled in HFSS with a frequency-dependent Drude dielectric constant given by

$$\epsilon_p = 1 - \frac{\omega_p^2}{\omega(\omega + i\nu)}, \tag{1}$$

where ω is the EM wave frequency, ν is the electron collisional damping rate, and ω_p is the plasma frequency, given by $\omega_p = \sqrt{n_e e^2 / m_e \epsilon_0}$ with n_e , e , and m_e being the column electron number density, electron charge, and electron mass, respectively, and ϵ_0 is the vacuum permittivity. As discussed below, based on comparisons between simulations and experiments, we believe that the fill pressure for the lamps used is somewhere in the vicinity of 100 Pa.

III. EXPERIMENTAL RESULTS

Figure 5 plots the experimental transmission for the plasma-off and plasma-on conditions of the device at nominal discharge voltage. The device has six somewhat identifiable attenuation bands, or “bandgaps” between 27 and 40 GHz, labeled BG_1 through BG_6 . These six bandgaps range in depth of their narrow attenuation features from about 10–25 dB below a 10–20 dB background. The structure surrounding the bands is greater in some vs others. For example, BG_1 and BG_3 are strong, narrow peaks whereas BG_2 , BG_4 , and BG_6 are shallow and more difficult to assign. BG_5 may be a collection of deep and narrow features. The transmission spectrum is complex, not atypical of a photonic crystal of finite size. For the plasma-on condition, the plasma frequency is much lower than the microwave field frequency and so the plasma will have only a subtle effect on the transmission in the vicinity of these resonances. Perhaps the most notable feature is the case of BG_5 , where there is an approximately 2–3 dB enhancement of the peak of the attenuation feature. In general, the difference between the plasma-on and plasma-off case is barely discernible in the figure. Despite this, we find that these small plasma-induced changes are regular and reproducible, and they are not attributable to thermal effects, as is discussed below. Measurements were taken for short times

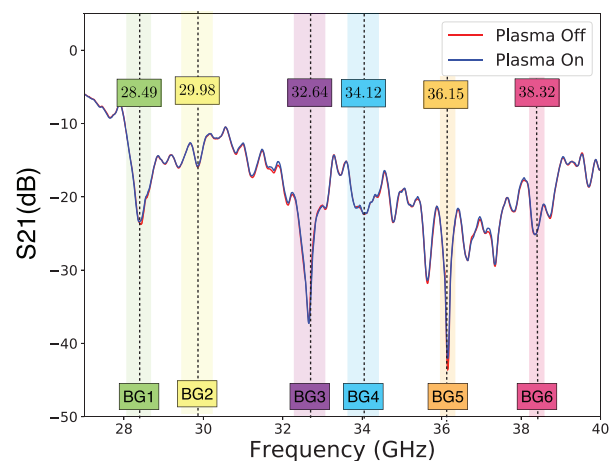


FIG. 5. Experimental transmission characteristics: Measured averaged ($N = 6$) free-space transmission (S_{21}) from 27 to 40 GHz had 6 characteristics bandgaps labeled BG_1 – BG_6 .

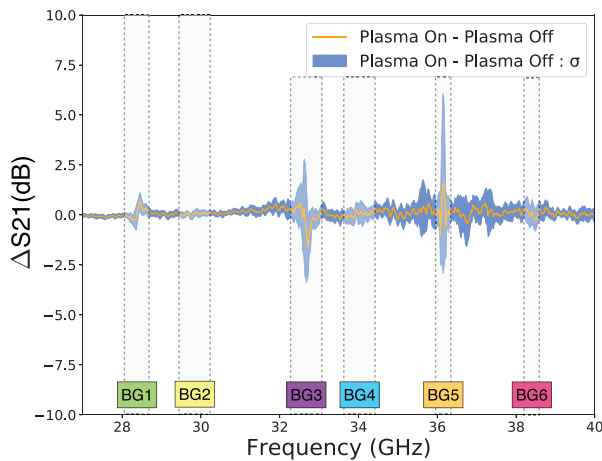


FIG. 6. Experimental differential transmission characteristics of the plasma on minus the plasma off conditions [Δ dB (plasma-on—plasma-off)] with standard deviation σ ($N = 6$) from 27 to 40 GHz with six characteristics bandgaps labeled BG_1 – BG_6 .

(~seconds) after the discharge is turned on from a cold start, and the temperature rise of the lamps (and therefore surrounding photonic crystal structure) is measurably small. Stronger effects are seen on the transmission spectra if we leave the plasma on for much longer times prior to recording the transmission. These stronger effects are attributed to thermal expansion of the scaffold. As shown below, the subtle variations seen here are consistent with nonthermal, plasma effects reproduced qualitatively in HFSS simulations. We emphasize that care must be taken to separate these thermal effects from pure plasma-related shifts in plasma photonic crystal experiments. Here, we systematically reduced the times at which the discharge is left on until we saw consistent and unchanging spectral variations that can only be attributed to the plasma density itself.

Figure 6 plots the experimental differential transmission (averaged over $N = 6$ scans) defined as the transmission with the plasma on minus the transmission with the plasma-off, along with the standard deviation of the N scans. We see that for some features there are distinct plasma-induced shifts. For example, The attenuation associated with BG_1 is “blue-shifted” by the plasma—discernable from the signoidal-like shape with a negative differential transmission at lower

frequency and positive differential transmission at higher frequencies. In contrast, the BG_3 shifts slightly toward the red and experiences a strong, nearly 2 dB strengthening of the attenuation. The attenuation feature associated with BG_5 seems to also be enhanced but also symmetrically broadened by the plasma. BG_2 , BG_4 , and BG_6 are affected to a lesser extent. Simulations are carried out to determine if a similar trend is seen and how it depends on properties such as the plasma frequency (plasma density). In this limit, changes in the transmission features were at most 1–5 dB in scale. These are rather small changes—much smaller than the changes seen in plasma photonic crystals that operate at frequencies closer to the plasma frequency.^{12,29–32}

The hybrid structure, which includes the dielectric spheres as well as the plasma and surrounding quartz envelope, is simulated using ANSYS HFSS 17.2 as an infinite photonic crystal along the x and z axis while applying a perfect magnetic boundary condition in the x – y plane and a perfect electric boundary condition in the x – z planes, as shown in Fig. 7(a) for a assumed plasma frequency of 7 GHz. Figure 7(b) shows a representative field calculation in the x – y plane. The effect of plasma density variations was investigated by varying plasma frequency. The collision frequency was set to 1 GHz, corresponding to the lower range predicted in the BOLSIG+ modeling and was held constant for all values of the plasma frequency. The simulations also predict the presence of six prominent bandgaps between 27 and 40 GHz, with attenuation feature depths and underlying background comparable to those very close in range to those seen experimentally, as shown in Fig. 8. The features in the simulations are more pronounced and free of nearby structures, in part because of the infinite size of the crystal due to the applied boundary conditions. Despite this difference, like the experiments, the attenuation bands range from 20 to 40 dB, on a background attenuation of 10–20 dB. Some notable differences are that BG_2 , BG_4 , and BG_6 are much more pronounced than what we see in the experiments, and BG_5 seems to be much broader, perhaps blending together the finer structures seen in the experimental transmission spectrum.

Figure 9 plots the differential transmission as a function of various plasma densities anticipated in the experiments. The underdense plasma layer expands the interspatial wave coupling between the two photonic crystal slabs due to the positive but less than 1 dielectric constant, allowing for a shifting in the location of the band edges. The hybrid device exhibits simulated responses that fall into three unique categories. The first, see, for example, BG_4 , is an attenuation band that

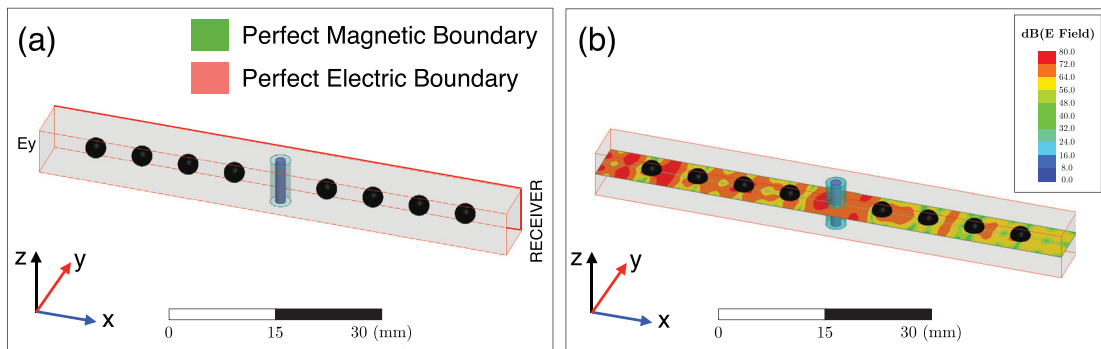


FIG. 7. (a) ANSYS HFSS Simulation domain with perfect magnetic boundary and perfect electric boundary conditions (b) E field cross section.

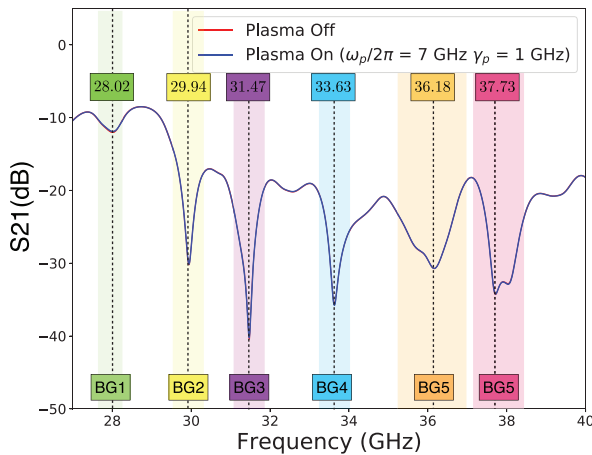


FIG. 8. Simulated transmission S_{21} (dB) of plasma on ($\omega_p/2\pi = 7$ GHz, $\gamma_p = 1$ GHz) and plasma off state of the hybrid plasma photonic crystal.

narrows significantly and asymmetrically with the onset of the plasma, and where the center of gravity shifts to lower frequency with increasing plasma density. The second, such as the bands associated with BG_1 and BG_2 , consists of a red (lower frequency)-shift with plasma onset, and a further increase in shift and in attenuation strength as plasma density is increased without a significant change in shape. It is noteworthy that this shift is opposite to that which we saw in the experiments. The feature labeled as BG_3 also falls into this category, but it is a more narrow feature and shifts toward the blue at low plasma density with increasing plasma density—hints of which were seen in the experiment. The third consists of peaks where the resonance is not affected by changes in plasma density in both location and intensity but can be switched on and off by turning on and off the plasma. BG_5 has a positive shift in frequency and the magnitude is not affected by changes in plasma density. A high frequency shift is seen in some of the features on the high frequency side of BG_1 in the experiments. BG_6

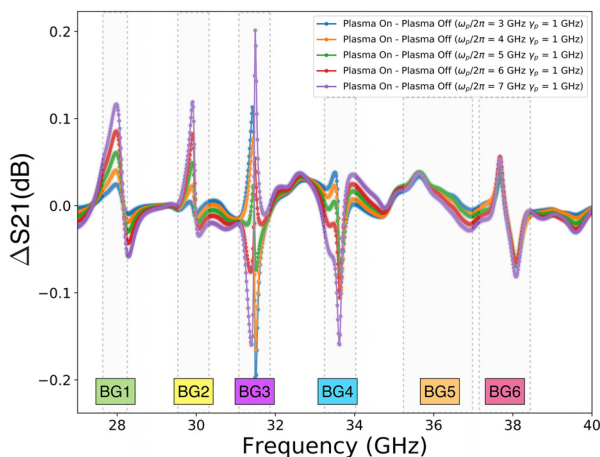


FIG. 9. Simulated differential transmission characteristics of the plasma-on minus the plasma-off conditions [Δ dB (plasma-on—plasma-off)] from 27 to 40 GHz with 6 characteristics bandgaps labeled BG_1 – BG_6 .

appears to undergo a negative shift, with a magnitude of the shift only slightly changed by plasma density. BG_6 may be the oddest of features, as it shifts for even low plasma density, but then becomes relatively insensitive to plasma density. BG_3 has the greatest differential magnitude that is positive at plasma frequency $\omega_p/2\pi = 3, 4,$ and 5 GHz and shifts negative in magnitude at 6 and 7 GHz. These simulated features are not due to thermal effects, as thermal expansion or heating is not accounted for in the HFSS simulations.

To better understand the structure of the field disturbances within the crystal and how the plasma influences propagation, we plot in Fig. 10 simulated E fields along the centerline of the crystal, intersecting the dielectric spheres and plasma, at three incident wave phases, $\Theta = 0^\circ, \Theta = 45^\circ, \Theta = 90^\circ$, and for the plasma off case, with frequencies corresponding to the center of all six attenuation features. This allows an examination of the response of the crystal structure to a moving wavefront. Figure 11 shows the corresponding differential E fields, i.e., the difference between plasma-on and plasma-off conditions ($\omega_p/2\pi = 7$ GHz, $\gamma_p = 1$ GHz), which visualizes where in the crystal the plasma-on condition has a greater effect on the propagation. The plasma and quartz elements couple the two photonic crystal components, and we can see that the plasma alters the coupling dynamics.

There is a distinct difference between the response of the three lower and three upper frequency features to the activation of the plasma. The lower three attenuation features, i.e., $BG_1, BG_2,$ and BG_3 , tend to have the E fields concentrated at the upstream interface of the quartz/plasma layer, with the E field intensity enhanced at the interface when the plasma is switched on. The field intensity is also high within the plasma elements at these three attenuation features. At these lower frequencies, the plasma presents a higher contrast in the refractive index, although the difference is expected to be small whereas the change in the characteristics between the lower and upper frequency features are rather abrupt. This suggests that there is a very distinct difference in these two groupings of resonance frequencies. The differential fields show that there is a high field concentration at the PLA-quartz interface at $\Theta = 0^\circ$, that seems to move to the quartz-plasma interface at $\Theta = 90^\circ$. These three features also seem to be PLA-mode dominated, with the fields concentrating in the PLA gap, enabling the quartz-plasma layer to better couple the two dielectric photonic crystal structures. It is apparent that at these frequencies, the plasma affects the fields on both sides of the quartz-plasma layer due to this PLA-mode coupling. This is an important feature for a device that requires the wavefronts to be modulated or manipulated, and the quartz-plasma layer is expected to modulate both the reflected and transmitted wavefronts.

In contrast, the upper three bandgap features, i.e., $BG_4, BG_5,$ and BG_6 , have fields that are less concentrated within the quartz and plasma, with the majority of the E fields concentrated in the high dielectric constant silicon nitride and lower fields in the PLA gaps. The wave propagation is still within the quartz-plasma elements as the wave propagates from the first photonic crystal to the second photonic crystal; however, the waves are already attenuated due to the first photonic crystal layer compared to BG_1 – BG_3 . The differential fields for BG_1 – BG_3 show small field shifts at the quartz-plasma interfaces, which is enough to shift the coupling of the two photonic crystals. The plasma is significantly affecting the fields in the first crystal near the E_y source, with less differential fields in the second half of the crystal. The quartz acts as a coupling element between the two photonic crystals,

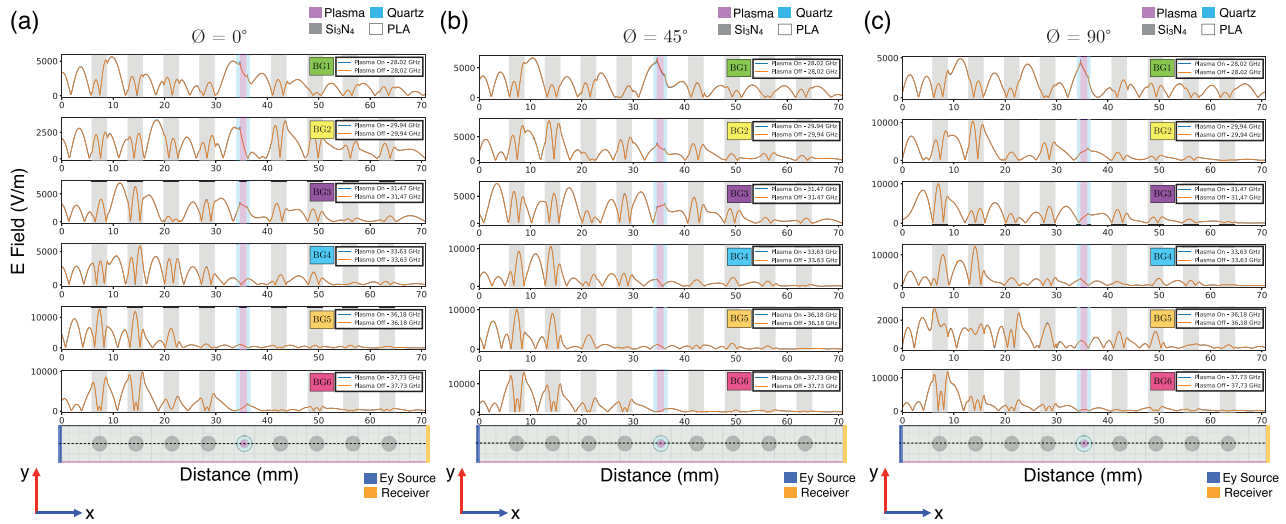


FIG. 10. XY cross-sectional E-fields along the centerline of the photonic crystal at phase: (a) $\Theta = 0^\circ$, (b) $\Theta = 45^\circ$, and (c) $\Theta = 90^\circ$ for each of the bandgap frequencies for plasma-on ($\omega_p/2\pi = 7$ GHz, $\gamma_p = 1$ GHz) and plasma-off conditions.

with the plasma changing the interfacial index contrast. For all of these band gaps, the plasma has a positive, but less than unity dielectric constant which increases the wavelength of waves within the plasma.

The XY plane cross-sectional E-field maps are shown for the plasma-on case in Fig. 12 and for the plasma-off case in Fig. 13. For BG_1 the plasma-off condition has fields concentrated at the inside of the quartz envelope, which is reduced in intensity when the plasma is turned on. BG_1 – BG_3 have a higher field concentration at the quartz-plasma element, with fields that also move around the cylindrical element. BG_4 has a lower field intensity inside the plasma and is dominated by fields located at the silicon nitride—PLA interface. BG_5 and

BG_6 have very low fields within the plasma, with the majority of the field concentrated on the left side near the source.

Figure 14 describes the results of a study that demonstrates the effects of increasing the discharge current (hence plasma density) on the transmission spectra and also how thermal effects can distort these spectra. In this study, we ramp up the discharge current from a cold start (plasma off and system at room temperature) starting at 2 A, keeping it there for 10 s, followed by an off state for 10 s. The discharge current is eventually increased to 2.8 A at 0.2 A steps with 10 s on followed by 10 s off. The entire experiment lasts for 110 s. During each off and on state, the transmission is recorded 2 s after the power is

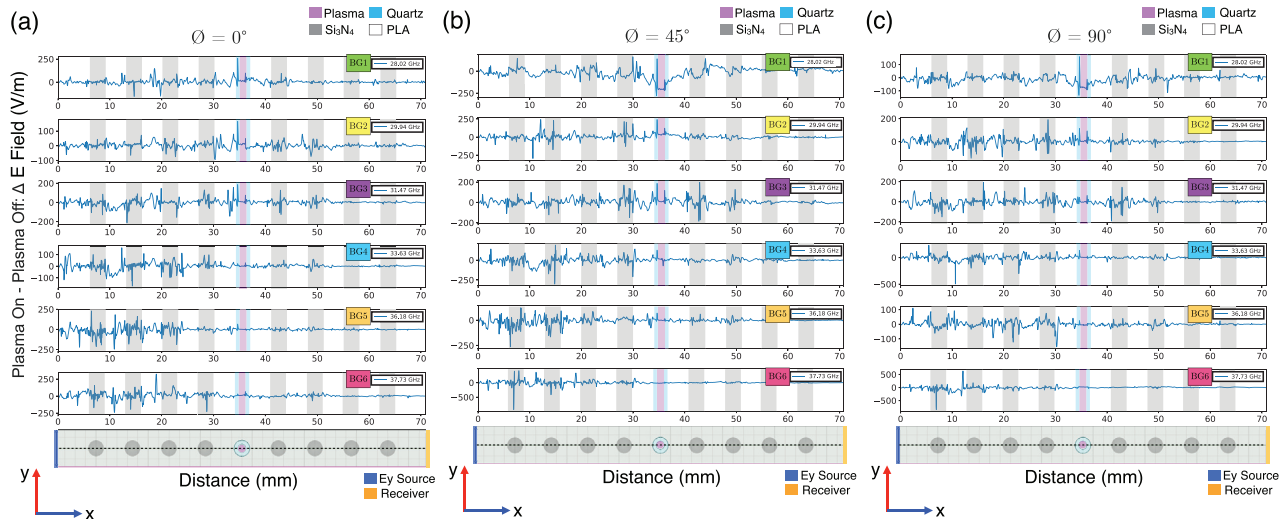


FIG. 11. XY differential (plasma-on—plasma-off) cross-sectional E-fields along the centerline of the photonic crystal at phase: (a) $\Theta = 0^\circ$, (b) $\Theta = 45^\circ$, and (c) $\Theta = 90^\circ$.

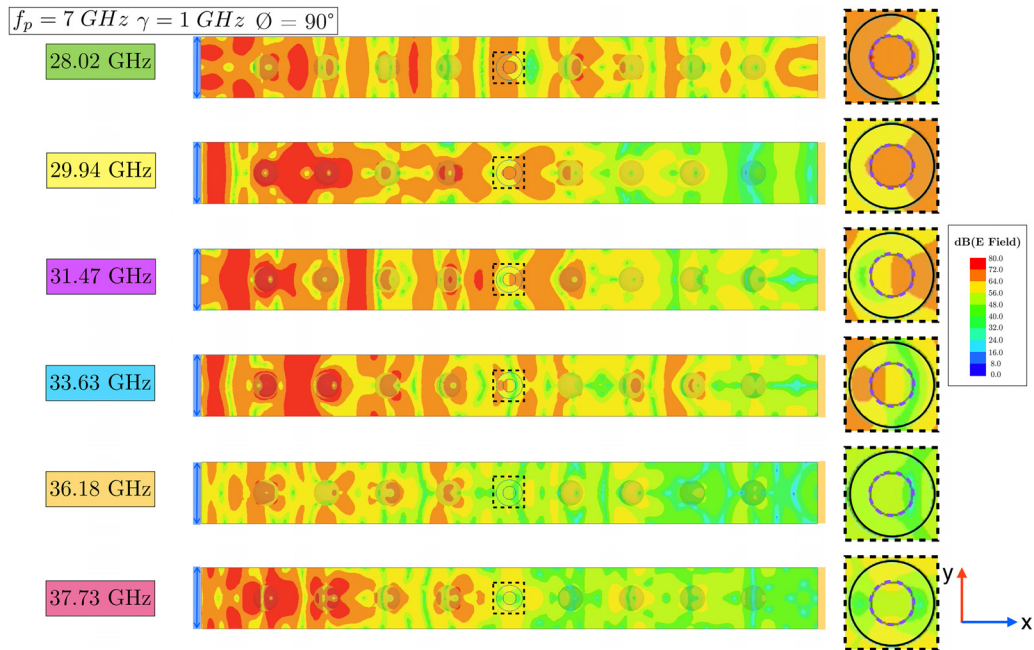


FIG. 12. XY plane cross-sectional E-fields for the plasma-on condition at the bandgap frequencies at $\varnothing = 90^\circ$.

turned on, and also after it is turned off. The experimental plan and the analysis of the transmission spectra are aided by the matrix at the bottom of the figure. It is noteworthy that the only time the system was at room temperature is before the start of the experiment, and so

off states are expectedly at higher temperatures as the 10 s off cases are not sufficient for the system to cooldown to room temperature. This is a rather thermally aggressive experiment in comparison to those for which the spectra have been shown earlier, where conditions were

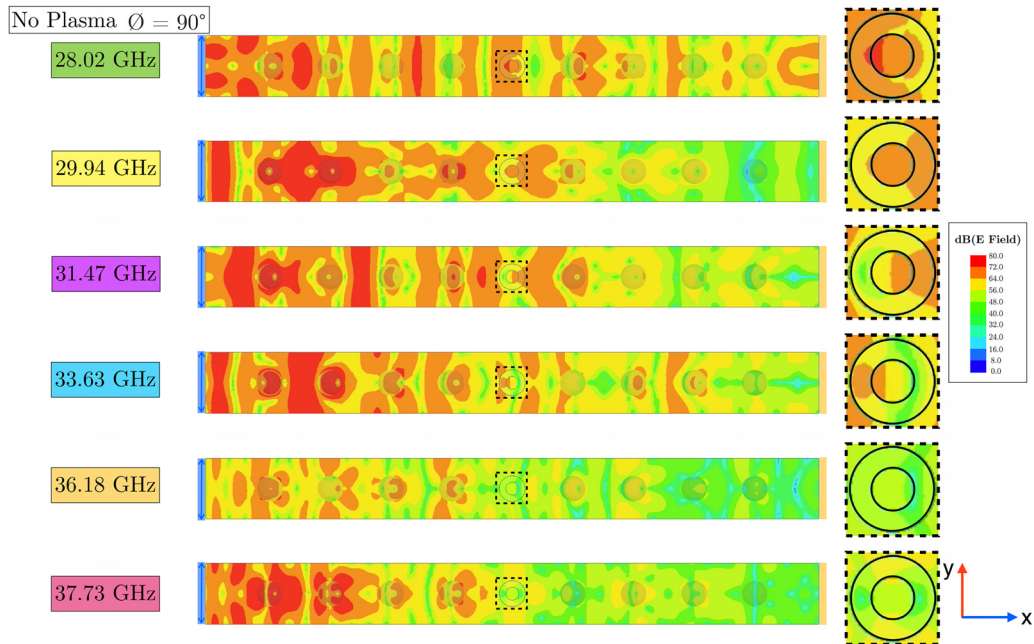


FIG. 13. XY plane cross-sectional E-fields for the plasma-off condition at the bandgap frequencies at $\varnothing = 90^\circ$.

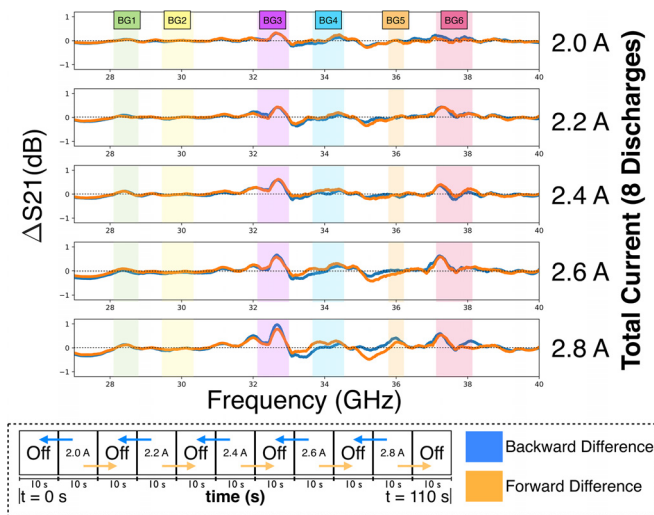


FIG. 14. Experimental transmission characteristics: measured free-space transmission (S_{21}) from 27 to 40 GHz at 5 different discharge currents.

such that the system was always close to room temperature. The temperature of the system was not measured during this particular 110 s of current ramp-up; however, the temperatures of similar studies were found to heat the ends of the discharge tubes to around 25 °C–30 °C, which suggests that the internal temperature of the device is even higher. At these higher temperatures, the thermal effects on the PLA scaffolds and quartz envelopes become apparent, as suggested by the analyzed spectra described below.

We study the behavior of the system by examining the differential spectrum determined by subtracting that spectrum recorded for each off state from the subsequent higher current spectrum collected with the plasma on. This represents the “backward difference” case, shown in blue in the matrix, and as the blue traces in the panel for the various discharge current cases. The second differential spectrum is that recorded with the plasma off from the spectrum recorded with the following plasma on state. This represents the “forward difference” case, shown in orange in the matrix, and as the orange traces in the figure for the various discharge current cases.

We would expect that the difference between the forward and backward differential spectra would be exacerbated as the current ramps up toward the 2.8 A condition, highlighting the increasing importance in the thermal effects. As we can see, the differential spectra recorded for the 2 and 2.2 A cases show only small differences between the forward and reverse difference curves. The differences are more pronounced at higher currents, reflecting the increased heating from these higher discharge current cases. It is interesting that the differences affect some of the attenuation bands more than the others. It seems that the higher frequency modes, BG_4 , BG_5 , and BG_6 , are more sensitive to thermal effects than the lower frequency modes. Consistent with the simulations, BG_1 exhibits an increase in the differential S_{21} with increasing plasma current. Experimentally BG_2 shows little change with increasing plasma current, consistent with Fig. 6, and in contrast with that of the simulations. BG_3 exhibits a more complex response, consistent with simulations increasing in both its differential S_{21} but also seems to experience a slight positive shift in center

frequency. All three of these attenuation bands do not seem to be strongly affected by temperature, as the orange and blue traces seem to be very similar. Of the higher frequency features, again, the BG_4 feature seems to change only slightly with increased current and its feature is quite weak in comparison to that suggested by the simulations. BG_5 has also a slight positive differential S_{21} at 2 A discharge current and appears to be weakly sensitive to increasing current consistent with simulations. Like BG_5 , BG_6 shows some sensitivity to current and at the highest current value is susceptible to thermal effects.

IV. DISCUSSION

Due to the rich coupling dynamics that we see between the plasma and dielectric elements within the device, we can conclude that a more robust iteration with slightly higher density plasma elements would serve as a good platform for EM wave manipulation and ANNs due to the potentially high level of nonlinearity and easy reconfigurability in continuous state space. The experimental realization of nonlinearity in glow discharge type plasmas driven by external field forcing without and with an external magnetic field has been explored experimentally.^{33,34} Ponderomotive force-induced nonlinearities have been investigated theoretically³⁵ and experimentally.³⁶ For our experiments, we anticipate strong nonlinearities due to external wave field forcing when the wave energy flux is in the range of 100 mW/cm², with ponderomotive-induced nonlinearities at somewhat higher levels. The shifting of the resonance bandgap peaks can be regulated by switching on and off of the plasma elements. The plasma elements are in an underdense configuration with a relative dielectric constant less than one but positive and can be tuned in the positive space by adjusting the plasma discharge current.

This platform could be trained using existing inverse design algorithms which are well-utilized in the field of electromagnetic devices. In a recent study,³⁷ we used computational methods and inverse design algorithms to train a similar plasma platform to perform functions such as demultiplexing and logic operations. Inverse design methodology may be particularly applicable to devices containing plasma elements due to the infinite configuration space that arises from the continuously reconfigurable plasma density of the elements. An example inverse design method is forward-mode differentiation³⁸ wherein the plasma current (and hence electron density) of each of the plasma elements is mapped to a set of parameters that are related to an objective, such as attenuation or transmission at a given frequency or field intensity in a given spatial location as defined by the user. The parameters are then varied while running the experiment either numerically or *in situ* to obtain gradients of the objective which can be used to optimize the device. Numerical simulations, while simpler to carry out, become costly as the various nonideal factors associated with the plasma sources are considered in order to maximize the chances of being able to experimentally realize the device with simulated parameters. Building a platform for experimental/*in situ* training of the device will likely lead to better performance but presents more of an engineering challenge. Both options are promising and represent a path for future work.

The 3D design of the crystal structure allows encoding of large amounts of information within the crystal by addressing each of the plasma elements individually. The ability to have a device that allows manipulation of wavefronts to be mapped to a potentially infinite state space of device configurations will provide a platform for one-shot

computing. Since the device is actively reconfigurable, photonic neural network devices can be realizable at the microwave frequency. The uniqueness of this approach comes from the use of underdense plasmas as tunable elements, utilizing the positive dielectric regime which has never before been fully explored. Future work will focus on making field measurements of the wavefronts at the receiver plane as a function of different plasma configurations and parameters. Ultimately, experiments carried out at high incident field power may reveal nonlinearities that might be exploited in these neural network applications.

ACKNOWLEDGMENTS

This research was partially supported by the Air Force Office of Scientific Research through a Multi-University Research Initiative (MURI) under Grant No. FA9550-14-1-0317 with Dr. Mitat Birkan as Program Manager. J.A.R. acknowledges the support from the U.S. Department of Energy, Office of Science, Office of Advanced Scientific Computing Research, Department of Energy Computational Science Graduate Fellowship, under Grant No. DE-SC0019323.

DATA AVAILABILITY

The data that support the findings of this study are available from the corresponding author upon reasonable request.

REFERENCES

- ¹A. D. McAulay, *Optical Computer Architectures: The Application of Optical Concepts to Next Generation Computers* (John Wiley & Sons, Inc., USA, 1991).
- ²K. Jain and G. W. Pratt, "Optical transistor," *Appl. Phys. Lett.* **28**(12), 719–721 (1976).
- ³B. Yegnanarayana, *Artificial Neural Networks* (PHI Learning Pvt. Ltd., 2009).
- ⁴Q. Zhang, H. Yu, M. Barbiero, B. Wang, and M. Gu, "Artificial neural networks enabled by nanophotonics," *Light: Sci. Appl.* **8**(1), 42 (2019).
- ⁵E. Khoram, A. Chen, D. Liu, L. Ying, Q. Wang, M. Yuan, and Z. Yu, "Nanophotonic media for artificial neural inference," *Photonics Res.* **7**(8), 823–827 (2019).
- ⁶I. A. Williamson, T. W. Hughes, M. Minkov, B. Bartlett, S. Pai, and S. Fan, "Reprogrammable electro-optic nonlinear activation functions for optical neural networks," *IEEE J. Sel. Top. Quantum Electron.* **26**(1), 1 (2020).
- ⁷T. W. Hughes, I. A. Williamson, M. Minkov, and S. Fan, "Wave physics as an analog recurrent neural network," *Sci. Adv.* **5**(12), eaay6946 (2019).
- ⁸Y. Takeoka, M. Honda, and T. Seki, "Dual tuning of the photonic band-gap structure in soft photonic crystals," *Adv. Mater.* **21**(18), 1801–1804 (2009).
- ⁹S. Zhang, Y. Xiong, G. Bartal, X. Yin, and X. Zhang, "Magnetized plasma for reconfigurable subdiffraction imaging," *Phys. Rev. Lett.* **106**(24), 243901 (2011).
- ¹⁰S. Mingaleev and Y. Kivshar, "Nonlinear photonic crystals toward all-optical technologies," *Opt. Photonics News* **13**(7), 48 (2002).
- ¹¹X. C. Sun, C. He, X. P. Liu, Y. Zou, M. H. Lu, X. Hu, and Y. F. Chen, "Photonic topological states in a two-dimensional gyrotropic photonic crystal," *Crystals* **9**(3), 137 (2019).
- ¹²B. Wang, J. Rodríguez, and M. A. Cappelli, "3d woodpile structure tunable plasma photonic crystal," *Plasma Sources Sci. Technol.* **28**(2), 02LT01 (2019).
- ¹³J. P. Lewicki, J. N. Rodriguez, C. Zhu, M. A. Worsley, A. S. Wu, Y. Kanarska, J. D. Horn, E. B. Duoss, J. M. Ortega, W. Elmer, R. Hensleigh, R. A. Fellini, and M. J. King, "3D-printing of meso-structurally ordered carbon fiber/polymer composites with unprecedented orthotropic physical properties," *Sci. Rep.* **7**, 43401 (2017).
- ¹⁴M. Mirzaee, S. Noghianian, L. Wiest, and I. Chang, "Developing flexible 3D printed antenna using conductive ABS materials," in Proceedings of IEEE International Symposium on Antennas and Propagation Society, AP-S (Digest) (2015), pp. 1308–1309.
- ¹⁵D. Chanda, K. Shigeta, S. Gupta, T. Cain, A. Carlson, A. Mihi, A. J. Baca, G. R. Bogart, P. Braun, and J. A. Rogers, "Large-area flexible 3D optical negative index metamaterial formed by nanotransfer printing," *Nat. Nanotechnol.* **6**(7), 402–407 (2011).
- ¹⁶B. Wang, R. Lee, R. Colon, and M. A. Cappelli, "A microstrip photonic crystal bandgap device with a switchable negative epsilon plasma element," *Microwave Opt. Technol. Lett.* **59**(12), 3097–3101 (2017).
- ¹⁷O. Sakai, T. Naito, and K. Tachibana, "Microplasma array serving as photonic crystals and plasmon chains," *Plasma Fusion Res.* **4**, 052 (2009).
- ¹⁸H. Hitoshi and A. Mase, "Dispersion relation of electromagnetic waves in one-dimensional plasma photonic crystals," *J. Plasma Fusion Res.* **80**(2), 89–90 (2004).
- ¹⁹J. Lo, J. Sokoloff, T. H. Callegari, and J. P. Boeuf, "Reconfigurable electromagnetic band gap device using plasma as a localized tunable defect," *Appl. Phys. Lett.* **96**(25), 251501 (2010).
- ²⁰M. A. Miri and A. Alù, "Exceptional points in optics and photonics," *Science* **363**(6422), eaar7709 (2019).
- ²¹J. Anderson, E. Kayraklioglu, S. Sun, J. Crandall, Y. Alkabani, V. Narayana, V. Sorger, and T. El-Ghazawi, "ROC: A reconfigurable optical computer for simulating physical processes," *ACM Trans. Parallel Comput.* **7**(1), 8 (2020).
- ²²V. Stefan, B. I. Cohen, and C. Joshi, "Nonlinear mixing of electromagnetic waves in plasmas," *Science* **243**(4890), 494–500 (1989).
- ²³R. Freer and I. O. Owate, "The dielectric properties of nitrides," in *The Physics and Chemistry of Carbides, Nitrides and Borides* (Springer, The Netherlands, Dordrecht, 1990), pp. 639–651.
- ²⁴G. J. Hagelaar and L. C. Pitchford, "Solving the Boltzmann equation to obtain electron transport coefficients and rate coefficients for fluid models," *Plasma Sources Sci. Technol.* **14**(4), 722–733 (2005).
- ²⁵See www.lxcat.net for SIGLO database.
- ²⁶A. Hilscher, "Determination of the cathode fall voltage in fluorescent lamps by measurement of the operating voltage," *J. Phys. D: Appl. Phys.* **35**(14), 1707–1715 (2002).
- ²⁷M. L. Huber, A. Laesecke, and D. G. Friend, "The vapor pressure of mercury," *Tech. Report No. 6643*, 2006.
- ²⁸U. E. P. Agency, "Ultraviolet disinfection guidance manual," EPA, Washington, D.C., Tech. Report No. EPA 815-D-03-007, 2003.
- ²⁹B. Wang and M. A. Cappelli, "A tunable microwave plasma photonic crystal filter," *Appl. Phys. Lett.* **107**(17), 171107 (2015).
- ³⁰B. Wang and M. A. Cappelli, "Waveguiding and bending modes in a plasma photonic crystal bandgap device," *AIP Adv.* **6**(6), 065015 (2016).
- ³¹B. Wang and M. A. Cappelli, "A plasma photonic crystal bandgap device," *Appl. Phys. Lett.* **108**(16), 161101 (2016).
- ³²F. Righetti, B. Wang, and M. A. Cappelli, "Enhanced attenuation due to lattice resonances in a two-dimensional plasma photonic crystal," *Phys. Plasmas* **25**(12), 124502 (2018).
- ³³D. Saha, P. K. Shaw, S. Ghosh, M. S. Janaki, and A. N. Sekar Iyengar, "Evidence of nonlinearity in presence of external forcing and magnetic field in a glow discharge plasma," *Chaos, Solitons Fractals* **98**, 46–55 (2017).
- ³⁴B. Sarma, S. S. Chauhan, A. M. Wharton, and A. N. Iyengar, "Comparative study on nonlinear dynamics of magnetized and un-magnetized dc glow discharge plasma," *Phys. Scr.* **88**(6), 065005 (2013).
- ³⁵Y. Wang, C. Yuan, Y. Liang, J. Yao, and Z. Zhou, "Ponderomotive force induced nonlinear interaction between powerful terahertz waves and plasmas," *Optik* **175**, 250–255 (2018).
- ³⁶H. Sobhani, H. R. Sabouhi, S. Feili, and E. Dadar, "Mode filtering based on ponderomotive force nonlinearity in a plasma filled rectangular waveguide," *Plasma Sci. Technol.* **19**(10), 105504 (2017).
- ³⁷J. A. Rodriguez, A. I. Abdalla, B. Wang, B. Lou, S. Fan, and M. A. Cappelli, "Inverse design of plasma metamaterial devices for optical computing," [arXiv:2102.05148](https://arxiv.org/abs/2102.05148) (2021).
- ³⁸T. W. Hughes, I. A. Williamson, M. Minkov, and S. Fan, "Forward-mode differentiation of Maxwell's equations," *ACS Photonics* **6**(11), 3010–3016 (2019).